

Measurement of the cosmic ray nickel energy spectrum from 10 GeV/n to 2 TeV/n with the DAMPE space mission

F. Alemanno, ^{1,2} Q. An, ^{3,4,*} P. Azzarello, ⁵ F. C. T. Barbato, ^{6,7} P. Bernardini, ^{1,2} X. J. Bi, ^{8,9} H. V. Boutin, ¹⁰ I. Cagnoli, ^{6,7} M. S. Cai, ^{10,11} E. Casilli, ^{6,7} J. Chang, ^{10,11} D. Y. Chen, ¹⁰ J. L. Chen, ¹² Z. F. Chen, ¹⁰ Z. X. Chen, ^{12,8} P. Coppin, ⁵ M. Y. Cui, ¹⁰ T. S. Cui, ¹³ I. De Mitri, ^{6,7} F. de Palma, ^{1,2} A. Di Giovanni, ^{6,7} T. K. Dong, ¹⁰ Z. X. Dong, ¹³ G. Donvito, ¹⁴ J. L. Duan, ¹² K. K. Duan, ¹⁰ R. R. Fan, ⁹ Y. Z. Fan, ^{10,11} F. Fang, ¹² K. Fang, ⁹ C. Q. Feng, ^{3,4} L. Feng, ¹⁰ S. Fogliacco, ^{6,7} J. M. Frieden, ^{5,†} P. Fusco, ^{14,15} M. Gao, ⁹ F. Gargano, ¹⁴ E. Ghose, ^{1,2} K. Gong, ⁹ Y. Z. Gong, ¹⁰ D. Y. Guo, ⁹ J. H. Guo, ^{10,11} S. X. Han, ¹³ Y. M. Hu, ¹⁰ G. S. Huang, ^{3,4} X. Y. Huang, ^{10,11} Y. Y. Huang, ¹⁰ M. Ionica, ¹⁶ L. Y. Jiang, ¹⁰ W. Jiang, ¹⁰ Y. Z. Jiang, ^{16,‡} J. Kong, ¹² A. Kotenko, ⁵ D. Kyratzis, ^{6,7} S. J. Lei, ¹⁰ B. Li, ^{10,11} M. B. Li, ⁵ W. L. Li, ¹³ W. H. Li, ¹⁰ X. Li, ^{10,11} X. Q. Li, ¹³ Y. M. Liang, ¹³ C. M. Liu, ¹⁰ H. Liu, ¹⁰ J. Liu, ¹² S. B. Liu, ^{3,4} Y. Liu, ¹⁰ F. Loparco, ^{14,15} M. Ma, ¹³ P. X. Ma, ¹⁰ T. Ma, ¹⁰ X. Y. Ma, ¹³ G. Marsella, ^{1,2,§} M. N. Mazziotta, ¹⁴ D. Mo, ¹² Y. Nie, ^{3,4} X. Y. Niu, ¹² A. Parenti, ^{6,7,¶} W. X. Peng, ⁹ X. Y. Peng, ¹⁰ C. Perrina, ^{5,†} E. Putti, ⁵ R. Qiao, ⁹ J. N. Rao, ¹³ Y. Rong, ^{3,4} A. Serpolla, ⁵ R. Sarkar, ^{6,7} P. Savina, ^{6,7} Z. Shangguan, ¹³ W. H. Shen, ¹³ Z. Q. Shen, ¹⁰ Z. T. Shen, ^{3,4} L. Silveri, ^{6,7,**} J. X. Song, ¹³ H. Su, ¹² M. Su, ¹⁷ H. R. Sun, ^{3,4} Z. Y. Sun, ¹² A. Surdo, ² X. J. Teng, ¹³ A. Tykhanov, ⁵ G. F. Wang, ^{3,4} J. Z. Wang, ⁹ L. G. Wang, ¹³ S. Wang, ¹⁰ X. L. Wang, ^{3,4} Y. F. Wang, ^{3,4} D. M. Wei, ^{10,11} J. J. Wei, ¹⁰ Y. F. Wei, ^{3,4} D. Wu, ⁹ J. Wu, ^{10,11,*} S. S. Wu, ¹³ X. Wu, ⁵ Z. Q. Xia, ¹⁰ Z. Xiong, ^{6,7} E. H. Xu, ^{3,4} H. T. Xu, ¹³ J. Xu, ¹⁰ Z. H. Xu, ¹² Z. Z. Xu, ^{3,4} Z. L. Xu, ¹⁰ G. F. Xue, ¹³ M. Y. Yan, ¹³ H. B. Yang, ¹² P. Yang, ¹² Y. Q. Yang, ¹² H. J. Yao, ¹² Y. H. Yu, ¹² Q. Yuan, ^{10,11} C. Yue, ¹⁰ J. J. Zang, ^{10,††} S. X. Zhang, ¹² W. Z. Zhang, ¹³ Y. Zhang, ¹⁰ Y. P. Zhang, ¹² Y. Zhang, ^{10,11} Y. J. Zhang, ¹² Y. Q. Zhang, ¹⁰ Y. L. Zhang, ^{10,3,4} Z. Zhang, ¹⁰ Z. Y. Zhang, ^{3,4} C. Zhao, ^{3,4} H. Y. Zhao, ¹² X. F. Zhao, ¹³ C. Y. Zhou, ¹³ X. Zhu, ^{10,‡‡} and Y. Zhu¹³

(DAMPE Collaboration)^{§§}

¹Dipartimento di Matematica e Fisica E. De Giorgi, Università del Salento, I-73100, Lecce, Italy

²Istituto Nazionale di Fisica Nucleare (INFN) - Sezione di Lecce, I-73100, Lecce, Italy

³State Key Laboratory of Particle Detection and Electronics,

University of Science and Technology of China, Hefei 230026, China

⁴Department of Modern Physics, University of Science and Technology of China, Hefei 230026, China

⁵Department of Nuclear and Particle Physics, University of Geneva, CH-1211, Switzerland

⁶Gran Sasso Science Institute (GSSI), Via Iacobucci 2, I-67100 L'Aquila, Italy

⁷Istituto Nazionale di Fisica Nucleare (INFN) - Laboratori Nazionali del Gran Sasso, I-67100 Assergi, L'Aquila, Italy

⁸University of Chinese Academy of Sciences, Beijing 100049, China

⁹Particle Astrophysics Division, Institute of High Energy Physics, Chinese Academy of Sciences, Beijing 100049, China

¹⁰Key Laboratory of Dark Matter and Space Astronomy,

Purple Mountain Observatory, Chinese Academy of Sciences, Nanjing 210023, China

¹¹School of Astronomy and Space Science, University of Science and Technology of China, Hefei 230026, China

¹²Institute of Modern Physics, Chinese Academy of Sciences, Lanzhou 730000, China

¹³National Space Science Center, Chinese Academy of Sciences,

Nanertiao 1, Zhongguancun, Haidian district, Beijing 100190, China

¹⁴Istituto Nazionale di Fisica Nucleare, Sezione di Bari, via Orabona 4, I-70126 Bari, Italy

¹⁵Dipartimento di Fisica “M. Merlin”, dell’Università e del Politecnico di Bari, via Amendola 173, I-70126 Bari, Italy

¹⁶Istituto Nazionale di Fisica Nucleare (INFN) - Sezione di Perugia, I-06123 Perugia, Italy

¹⁷Department of Physics and Laboratory for Space Research,

the University of Hong Kong, Hong Kong SAR, China

(Dated: December 15, 2025)

Nickel, one of the most stable elements alongside iron, is the most abundant heavy element beyond iron in cosmic rays. With DAMPE’s excellent charge resolution and broad energy range, a high-precision energy spectrum provides valuable insights into the acceleration sources of heavy nuclei and their propagation through the interstellar medium. In this analysis, we report the direct measurement of cosmic-ray nickel spectrum from 10 GeV/n to 2 TeV/n with nine years of flight data. The nickel spectrum is consistent with a single power law with spectral index -2.60 ± 0.03 from 40 GeV/n to 1 TeV/n. This work provides an accurate measurement of differential flux of nickel with kinetic energy extending to TeV/n for the first time.

Introduction - Galactic cosmic rays, discovered by Hess in 1913, are high-energy particles originating from outer space and traversing the Galaxy. They can serve as valuable probes for exploring astrophysical particle accelerators and the in-

terstellar medium of the Galaxy [1]. According to the first order Fermi acceleration mechanism and diffusive transportation, the energy spectra of cosmic-ray nuclei follows a single power law [2]. However, with the accumulation of observed

data and the expansion of energy range, many experiments indicate that the spectra of cosmic rays exhibit deviations from a single power law in the energy range around hundreds of GeV/n for proton, helium, and other heavy primary nuclei in cosmic rays [3–15].

Heavy nuclei observed in cosmic rays primarily originate from stellar nuclear fusion process [16]. Iron, with the highest binding energy per nucleon among all stable nuclei, is the most abundant element among nuclei heavier than silicon. The spectrum shape around TeV/n of iron was reported by several experiments such as AMS-02 [11], CALET [15] and NUCLEON [17]. Although there are several theoretical models about the synthesis, acceleration and propagation of heavy nuclei in cosmic rays [16, 18–21], current observational results for nickel and heavier nuclei mainly focus on relative abundance measurements [22, 23]. Even about nickel, the most abundant species in this trans-iron group, only a few experiments, such as CRYSIS [24], HEAO3-C2 [25] and Balloon [26], provided differential energy spectrum in the low energy region below 40 GeV/n. Besides these, the CALET experiment reported the energy spectrum from 8.8 GeV/n to 240 GeV/n [27], while the NUCLEON reported the upper limit at 511 GeV/n [28]. However, these results are not entirely consistent. Consequently, a precise measurement in the high-energy region is still needed.

The DArk Matter Particle Explorer (DAMPE, also known as "Wukong" in China), is a calorimetric-type, satellite-borne detector with the goal to observe the high-energy electrons, gamma rays, and cosmic rays [29], launched into a 500-km Sun-synchronous orbit on December 17th, 2015. From top to bottom, DAMPE consists of a Plastic Scintillator Detector (PSD) [30–33], a Silicon-Tungsten tracKer converter (STK) [34, 35], a Bismuth Germanate (BGO) imaging calorimeter [36, 37], and a NeUtron Detector (NUD) [38]. The PSD measures the charges of incident particles and contributes to the anti-coincidence measurement of gamma rays. The STK reconstructs the trajectory and provides additional charge measurements for light nuclei. The BGO calorimeter measures the energy and trajectory of incident particles and discriminates electrons and photons effectively from hadrons based on their shower profiles. The NUD is used for additional electron/proton discrimination. The calibration with nine-year on-orbit data reveals that DAMPE has excellent stability [39–42]. Due to its large acceptance and wide energy range, the DAMPE detector is expected to contribute to the study of high-energy heavy nuclei in cosmic rays.

In this Letter, the measurement of the nickel spectrum with kinetic energy from 10 GeV/n to 2 TeV/n is reported. Our results are the first to extend the energy coverage for the nickel spectrum up to TeV/n.

Data analysis - This analysis utilized nine years of data collected by DAMPE between January 1, 2016 and December 31, 2024. After subtracting instrumental dead time, on-orbit calibration time, a giant solar flare between September 9 and September 13, 2017 [43], and the South Atlantic Anomaly (SAA) passage time [39], the total exposure time was deter-

mined to be 2.17×10^8 s, about 76% of the total operational duration.

The Geant4 toolkit (version 4.10.5) [44] was used to simulate the response of the DAMPE detector to different particles. For nickel nuclei with primary energies between 100 GeV and 10 TeV, the simulation implemented FTFP_BERT model, and for energy above 10 TeV, the EPOS-LHC model [45] which was linked to the Geant4 with the cosmic ray Monte Carlo (CRMC) package [46, 47]. Particles were generated from a hemispherical isotropic source surrounding the detector with a power-law energy spectrum (index $\gamma = -1$). The primary particle sample consisted of ^{58}Ni and ^{60}Ni , mixed in a ratio of 5:2 [48–50]. Besides, there was also a simulation based on FLUKA 2011.2x [51] to evaluate systematic uncertainty from hadronic interaction model.

(i) *Preselection* - To identify nickel candidate events from cosmic rays and reconstruct the kinetic energy spectrum, firstly the trajectories and charges of incident particles are required to be well reconstructed. Several selection criteria were applied to extract a high-purity sample of nickel candidates for kinetic energy reconstruction. In this analysis, deposited energy in BGO (E_{dep}) was required to be more than 100 GeV, thereby avoiding the effects of the geomagnetic effect on low energy particles [52]. Only events passing High Energy Trigger were analyzed [53]. For nickel with kinetic energy above 10 GeV/n, the trigger efficiency was nearly 100%.

(ii) *Track selection* - A method of track reconstruction using machine learning was developed to avoid efficiency loss for heavy nuclei caused by saturation effect and common-mode noise compression in STK [54]. This method maintains high efficiency even when the deposited energy in BGO exceeds 10 TeV. And the PSD charges along the track must exhibit the highest deposited energy among the adjacent four PSD strips in both PSD-x and PSD-y layer. Additionally, particle trajectories must be incident on the top surface of the PSD detector and traverse the BGO calorimeter, through both of its top and bottom surface. To suppress edge effects, the strip with the maximum deposited energy in each layer of the BGO calorimeter should not be the outmost one.

(iii) *Charge selection* - The PSD detector is mainly used for charge measurement. Charge reconstruction is based on ionization energy loss in PSD, scaling with the square of the particle charge according to the Bethe-Bloch formula. The charge value obtained has been corrected to eliminate position dependence, light attenuation, quenching effects and energy dependence [31, 32]. Because the PSD detector is composed of four sub-layers, two sub-layers aligned in yz view and two in xz view, requiring particles to traverse at least three sub-layers of PSD detector is feasible to improve charge resolution. To guarantee the consistency of different PSD layers, the variance of these charge values in each PSD layer was required to be less than 1.2 as shown in FIG.S1 of Supplemental Material (SM) [55]. A global PSD charge, detailed in the SM [55] with charge resolution of 0.37 e for nickel is used for charge identification. Figure.1 shows the PSD charge distributions for deposited energy bins, 100 - 158 GeV and 4.64 - 10 TeV.

The charge selection window for nickel was set from 27.6 to 28.8, with approximately 80% selection efficiency. A total of over 59k candidate events were collected with deposited energy ranging from 100 GeV to 100 TeV.

(iv) *Background subtraction* - To estimate the contamination from other nuclei, a template fit was performed based on the simulation. The MC charge spectra from chromium to zinc after smearing are also shown in FIG.1 with different colored dashed lines. The dominate sources of contamination were iron, cobalt, and copper. Among these sources, cobalt was the highest, accounting for 2% at the deposited energy of 100 GeV and 10% at 100 TeV. The estimated contamination fractions from different nuclei are shown in FIG.S3 of SM [55]. Contributions from other nuclei exhibited energy dependence, varying from 4% at the deposited energy of 100 GeV to 20% at 100 TeV. The background from nuclei heavier than zinc could be ignored because of low abundance.

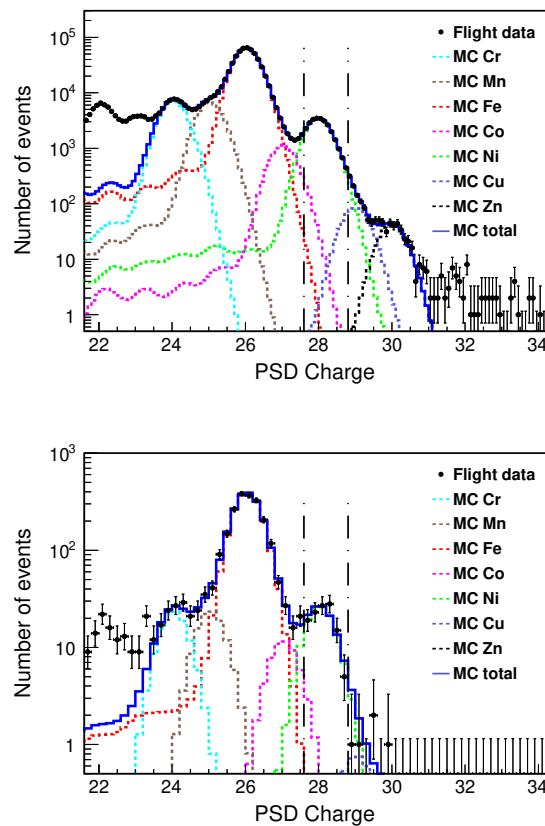


FIG. 1: The distribution of PSD Charge of flight data (black points) within deposited energy bins of 100 - 158 GeV (top) and 4.64 - 10 TeV (bottom). The result of template fits is shown as the blue line, and the other nuclei as different colored dashed lines.

Effective acceptance - The effective acceptance after selec-

tion in the i -th incident energy bin was calculated as

$$A_{\text{eff},i} = A_{\text{gen}} \times \frac{N_{\text{pass},i}}{N_{\text{gen},i}}. \quad (1)$$

A_{gen} is the geometrical factor of MC events generator. In the i -th kinetic energy bin, $N_{\text{pass},i}$ is the number of events passing selection and $N_{\text{gen},i}$ is the total number of events generated. The effective acceptance as the function of kinetic energy is approximately $0.07 \text{ m}^2\text{sr}$ above 10 GeV/n (see FIG.S4 in the SM [55]).

Energy measurement and unfolding procedure - In this analysis, the total deposited energy in BGO calorimeter was used for energy measurement. For a BGO crystal with energy deposited over 10 TeV, its readout electronics would saturate. To mitigate the impact of saturation effects on energy measurement, a correction algorithm based on MC simulation was performed [58]. The Birks' quenching effect in BGO crystal was took into account in the MC simulations [59, 60]. This effect primarily affected the measurement of nickel spectra in low energy region below 100 GeV/n.

Due to limited 1.6 nuclear interaction length of the BGO calorimeter, ion particles deposit approximately 30% of their kinetic energy with a certain degree of broadening within BGO calorimeter [61]. The relationship between the number of events in i -th deposited energy bin $N(E_{\text{dep}}^i)$ and the number of events in j -th incident kinetic energy bin $N(E_{\text{inc}}^j)$ is formulized as

$$N(E_{\text{dep}}^i) = \sum_{j=1}^n P(E_{\text{dep}}^i | E_{\text{inc}}^j) N(E_{\text{inc}}^j). \quad (2)$$

$P(E_{\text{dep}}^i | E_{\text{inc}}^j)$ represents the energy response matrix, derived from MC simulations. A Bayesian unfolding method [62] was employed to convert the deposited energy spectrum back to the incident kinetic energy spectrum.

Flux calculation - The differential flux spectrum for nickel was calculated using the following formula:

$$\Phi_i = \Phi(E_{\text{inc}}^i, E_{\text{inc}}^i + \Delta E_i) = \frac{N_{\text{inc}}^i}{\Delta E_i T_{\text{exp}} A_{\text{eff},i}}. \quad (3)$$

In i -th incident kinetic energy bin, ΔE_i is the width of the bin and N_{inc}^i is the number of events after unfolding. $A_{\text{eff},i}$ is the effective acceptance and T_{exp} is the exposure time. The fluxes are then expressed as kinetic energy per nucleon assuming the isotopic ratio of $^{58}\text{Ni} : ^{60}\text{Ni} = 5 : 2$.

Uncertainty analysis - The statistical uncertainty mainly originated from Poisson fluctuations of the number of observed events $N(E_{\text{dep}}^i)$. A toy-MC approach was applied in each deposited energy bin based on Poisson distribution. The statistical uncertainty was then evaluated by calculating the root-mean-square of distribution in the corresponding kinetic energy bins.

The sources of systematic uncertainties in the nickel analysis are complex, including selection efficiency, background

subtraction, hadronic model, unfolding procedure and isotopic assumption. Comparing MC simulation with flight data, the difference was negligible for high energy trigger efficiency and within 0.5% for track efficiency (see the FIG.S5 in SM [55]). The uncertainty of charge selection was evaluated by adjusting the charge selection window from -0.1 to +0.2 corresponding to a variation of charge selection efficiency of 10%. The flux in kinetic energy bins varied by 1% at 10 GeV/n and 7% at 1 TeV/n. The uncertainty of background subtraction was evaluated by varying the contamination level by 50%. The differential flux of nickel would vary about 2% at 10 GeV/n and 7% at 1 TeV/n.

There are several selection criteria associated with charge reconstruction which should be considered into the source of systematic uncertainties. The systematic error associated with the requirement for matching STK track with PSD maximum energy strip was assessed by relaxing this condition and examining the variation of results. This caused a nickel flux variation less than 1% at 10 GeV/n and 8% at 1 TeV/n. A comparative study on the charge consistency efficiency was conducted showing the difference between flight data and MC simulation was less than 4% (see the FIG.S2 in the SM [55]).

The main source of systematic uncertainty below 200 GeV/n is the hadronic model. Below 75 GeV/n, the difference between beam test data and simulation based on GEANT4 was attributed to the hadronic model uncertainty detailed in the FIG.S6 of SM [55]. Above 75 GeV/n, an independent analysis based on FLUKA was used to compare with the results based on GEANT4. This difference was about 6% at 1 TeV/n. The systematic uncertainty from unfolding procedure caused by the initial index and the MC sample in unfolding matrix was estimated to be less than 1%. Based on past isotopic observations, a variation of 15% in the ^{60}Ni abundance would bring 0.8% difference into the result of nickel flux [48–50]. Total uncertainties including statistical uncertainty and systematic uncertainties from different sources in different kinetic energy bin are shown in FIG.S7 of the SM.

Results - Figure. 2 shows the differential nickel spectrum in kinetic energy per nucleon from 10 GeV/n to 2 TeV/n. A softening feature is observed around 40 GeV/n which is similar to other nuclei like proton, helium or iron [3–15]. A fit with a single power law function (SPL)

$$\Phi(E) = \Phi_0 \left(\frac{E}{1\text{GeV}/n} \right)^\gamma \quad (4)$$

was performed to the nickel flux with kinetic energy from 40 GeV/n to 1 TeV/n. The index γ of spectrum is -2.60 ± 0.03 with a $\chi^2/\text{dof} = 0.40/3$. Because of the limited statistics above 1 TeV/n, whether the nickel flux above TeV/n still follows a single power law remains to be verified.

The variation of the nickel to iron ratio with incident energy was also shown in FIG. 3. A constant fit from 10 GeV/n to 2 TeV/n gives a constant value of 0.057 ± 0.002 with a $\chi^2/\text{dof} = 2.12/7$. In this work, the nickel to iron ratio measured by DAMPE is structurally consistent with previous

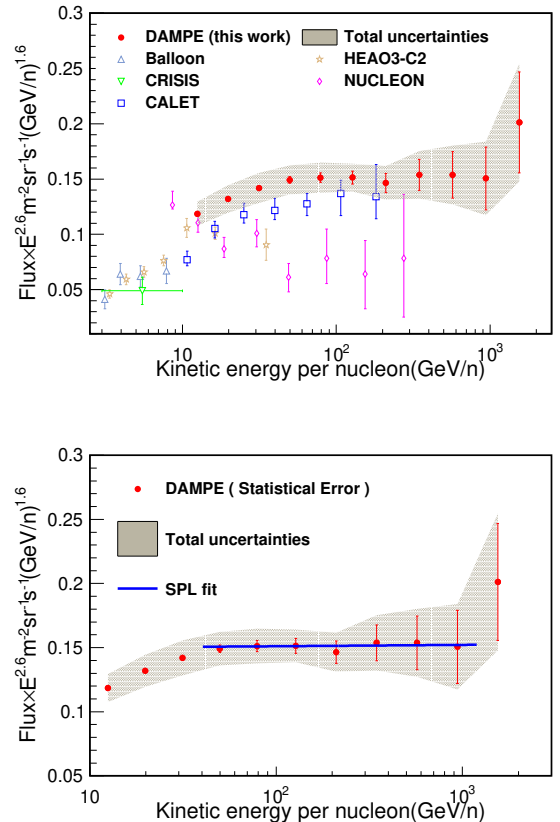


FIG. 2: Nickel spectrum weighted by $E^{2.6}$ measured by DAMPE (converted to kinetic energy per nucleon assuming the isotopic composition of $A = 58.57$). The nickel spectrum measured by DAMPE was compared with the previous results by Balloon 1975 [26], CRISIS [24], HEAO3-C2 [25], NUCLEON [28] and CALET [27]. The red bars represent the statistical uncertainty. The outer shaded bands represents the total uncertainties including statistical and systematic uncertainties from analysis procedure and hadronic model. Bottom panel: The fit of the nickel spectrum in the energy range [40 GeV/n, 1 TeV/n] with an SPL function (blue line).

CALET measurements in the same energy range with a systematic shift of an absolute value.

Conclusion - In this Letter, the nickel spectrum from 10 GeV/n to 2 TeV/n is measured with nine years of data collected by DAMPE. There is a similar softening as lighter nuclei around 40 GeV/n in nickel flux. The nickel spectrum measured by DAMPE is well consistent with a SPL fit above 40 GeV/n which gives a spectra index $\gamma = -2.60 \pm 0.03$. In the energy region from 10 GeV/n to 2 TeV/n, the nickel to iron ratio can be approximately described by a constant 0.057 ± 0.002 . In theory, iron and nickel are mainly synthesized thermonuclear explosions of supernovae, as well as in Si-burning during explosive burning of core-collapse supernovae [63–66]. Based on current models and observational data, the nickel to iron

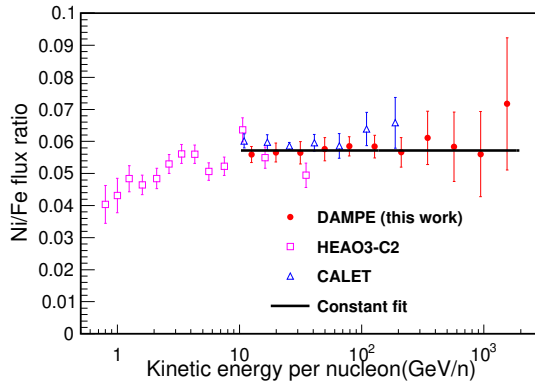


FIG. 3: Nickel to iron flux ratio measured by DAMPE (red points) fit with a constant function (black line). The red bars represent the total uncertainty including statistical uncertainty and systematic uncertainties. The blue points show the measurements from CALET. The pink points shows the measurements from HEAO3-C2.

yield ratio seems stable in the source region. The constant Ni/Fe abundance ratio in cosmic rays further indicates the similar origin, acceleration and propagation mechanism for both elements. A hardening structure was observed for iron at kinetic energy 512.5 GeV/n [67]. For nickel at kinetic energy above hundreds of GeV/n, current statistics are not enough to draw a definitive conclusion. Our measurements represent the first observation of the nickel energy spectrum extending to TeV/n with a higher precision than most of existing experimental results. The accumulating DAMPE dataset would facilitate more precision measurements of nickel extending to higher energy.

Acknowledgment - The DAMPE mission was funded by the strategic priority science and technology projects in space science of Chinese Academy of Sciences (CAS). In China, the data analysis was supported by the National Key Research and Development Program of China (No. 2022YFF0503303) and the National Natural Science Foundation of China (Nos. 12220101003, 12588101, 12003076 and 12022503), the CAS Project for Young Scientists in Basic Research (Nos. YSBR-061 and YSBR-092), the Strategic Priority Program on Space Science of Chinese Academy of Sciences (No. E02212A02S), the Youth Innovation Promotion Association of CAS, the Young Elite Scientists Sponsorship Program by CAST (No. YESS20220197), and the Program for Innovative Talents and Entrepreneur in Jiangsu and the NSFC under grant (No. 12588101). Y.Z. F thanks the support of New Cornerstone Science Foundation through the XPLORERPRIZE. In Europe, the activities and data analysis are supported by the Swiss National Science Foundation (SNSF), Switzerland, the National Institute for Nuclear Physics (INFN), Italy, and the European Research Council (ERC) under the European Union's Horizon 2020 research and innovation programme

(No. 851103), and the Swiss State Secretariat for Education, Research and Innovation (SERI).

* Deceased

† Now at Institute of Physics, Ecole Polytechnique Fédérale de Lausanne (EPFL), CH-1015 Lausanne, Switzerland.

‡ Also at Dipartimento di Fisica e Geologia, Università degli Studi di Perugia, I-06123 Perugia, Italy.

§ Now at Dipartimento di Fisica e Chimica “E. Segrè”, Università degli Studi di Palermo, via delle Scienze ed. 17, I-90128 Palermo, Italy.

¶ Now at Inter-university Institute for High Energies, Université Libre de Bruxelles, B-1050 Brussels, Belgium.

** Now at New York University Abu Dhabi, Saadiyat Island, Abu Dhabi 129188, United Arab Emirates.

†† Also at School of Physics and Electronic Engineering, Linyi University, Linyi 276000, China.

‡‡ Also at School of computing, Nanjing University of Posts and Telecommunications, Nanjing 210023, China.

§§ dampe@pmo.ac.cn

- [1] I. A. Grenier, J. H. Black, and A. W. Strong, *Annu. Rev. Astron. Astrophys.* **53**, 199 (2015).
- [2] E. Fermi, *Phys. Rev.* **75**, 1169 (1949).
- [3] A. D. Panov *et al.* (ATIC), *Bull. Russ. Acad. Sci. Phys.* **73**, 564 (2009).
- [4] Y. S. Yoon *et al.* (CREAM), *Astrophys. J.* **839**, 1 (2017).
- [5] O. Adriani *et al.* (PAMELA), *Science* **332**, 69 (2011).
- [6] O. Adriani *et al.* (PAMELA), *Adv. SpaceRes.* **51**, 219 (2013).
- [7] M. Aguilar *et al.* (AMS), *Phys. Rev. Lett.* **114**, 171103 (2015).
- [8] M. Aguilar *et al.*, *Phys. Rev. Lett.* **124**, 211102 (2020).
- [9] M. Aguilar *et al.* (AMS), *Phys. Rev. Lett.* **115**, 211101 (2015).
- [10] M. Aguilar *et al.* (AMS), *Phys. Rev. Lett.* **119**, 251101 (2017).
- [11] M. Aguilar *et al.* (AMS), *Phys. Rev. Lett.* **126**, 041104 (2021).
- [12] Q. An, R. Asfandiyarov, P. Azzarello, *et al.* (DAMPE), *Science Advances* **5**, eaax3793 (2019).
- [13] F. Alemanno, Q. An, P. Azzarello, *et al.* (DAMPE), *Phys. Rev. Lett.* **126**, 201102 (2021).
- [14] O. Adriani *et al.* (CALET), *Phys. Rev. Lett.* **122**, 181102 (2019).
- [15] O. Adriani *et al.* (CALET), *Phys. Rev. Lett.* **126**, 241101 (2021).
- [16] E. M. Burbidge, G. R. Burbidge, W. A. Fowler, and F. Hoyle, *Rev. Mod. Phys.* **4**, 29 (1957).
- [17] V. Grebenyuk *et al.*, *Adv. Space Res.* **64**, 2546 (2019).
- [18] S. E. Woosley and T. A. Weaver, *Astrophys. J. Suppl. Ser.* **1**, 101 (1995).
- [19] **245** (2019).
- [20] N. Tomassetti, *Astrophys. J. Lett.* **752**, L13 (2012).
- [21] M. J. Boschini, S. D. Torre, M. Gervasi, D. Grandi, G. Jóhannesson, G. L. Vacca, *et al.*, *Astrophys. J. Suppl. Ser.* **250**, 27 (2020).
- [22] R. P. Murphy *et al.*, *Astrophys. J.* **831**, 2 (2016).
- [23] W. R. Binns, M. E. Wiedenbenck, T. T. V. Rosenvinge, *et al.*, *Astrophys. J.* **936**, 13 (2022).
- [24] J. S. Young, P. S. Freier, C. J. Waddington, N. R. Brewster, and R. K. Fickle, *Astrophys. J.* **1014**, 246 (1981).
- [25] J. J. Engelmann *et al.*, *Astron. Astrophys.* **233**, 96 (1990).
- [26] G. Minagawa *et al.*, *Astrophys. J.* **248**, 847 (1981).
- [27] O. Adriani *et al.* (CALET), *Phys. Rev. Lett.* **128**, 131103 (2022).

[28] V. Grebenyuk *et al.* (NUCLEON), arXiv:1809.07285. .

[29] J. Chang, G. Ambrosi, Q. An, *et al.* (DAMPE), *Astropart. Phys.* **95**, 6 (2017).

[30] Y. H. Yu *et al.*, *Astropart. Phys.* **94**, 1 (2017).

[31] M. Ding *et al.*, *Res. Astron. Astrophys.* **19**, 047 (2019).

[32] T. K. Dong *et al.*, *Astropart. Phys.* **105**, 31 (2019).

[33] P. X. Ma, M. Di Santo, Z. H. Xu, Y. L. Zhang, *et al.* (DAMPE), *Pos ICRC2021*, 395 (2021).

[34] P. Azzarello *et al.*, *Nucl. Instrum. Meth. A* **831**, 378 (2016).

[35] A. Tykhonov *et al.*, *Nucl. Instrum. Meth. A* **893**, 43 (2018).

[36] Z. Zhang *et al.*, *Nucl. Instrum. Meth. A* **836**, 98 (2016).

[37] L. Wu *et al.*, *IEEE Trans. Nucl. Sci.* **65**, 2007 (2018).

[38] Y. Y. Huang *et al.*, *Res. Astron. Astrophys.* **20**, 153 (2020).

[39] G. Ambrosi *et al.* (DAMPE), *Astropart. Phys.* **106**, 18 (2019).

[40] P. X. Ma *et al.*, *Res. Astropart. Phys.* **19**, 082 (2019).

[41] A. Tykhonov *et al.*, *Nucl. Instrum. Meth. A* **924**, 309 (2019).

[42] C. M. Liu *et al.*, *IEEE Trans. Nucl. Sci.* **70**, 1288 (2023).

[43] <https://solarflare.njit.edu/datasources.html>.

[44] S. Agostinelli *et al.*, *Nucl. Instrum. Meth. A* **506**, 250 (2003).

[45] T. Pierog, I. Karpenko, J. M. Katzy, E. Yatsenko, and K. Werner, *Phys. Rev. C* **92**, 034906 (2015).

[46] <https://web.ikp.kit.edu/rulrich/crmc.html>.

[47] A. Tyhonov, D. Droz, C. Yue, M. Cui, X. Li, and X. Wu (DAMPE), *Pos ICRC2019*, 143 (2021).

[48] J. J. Connell and J. A. Simpson, *Astrophys. J.* **475**, 1 (1997).

[49] A. Lukasial, F. B. McDonald, W. R. Webber, and P. Ferrando, *Adv. Space. Res.* **19**, 747 (1997).

[50] M. E. Wiedenbeck *et al.*, *Adv. Space. Res.* **27**, 773 (2001).

[51] T. Böhlen, F. Cerutti, M. Chi, A. Fassò, A. Ferrari, P. Ortega, A. Mairani, P. Sala, G. Smirnov, and V. Vlachoudis, *Nucl. Data. Sheets* **120**, 211 (2014).

[52] E. Thébault *et al.*, *Earth Planets Space* **67**, 79 (2015).

[53] Y. Q. Zhang, J. H. Guo, Y. Liu, C. Q. Feng, Y. L. Zhang, T. K. Dong, J. J. Zang, and C. Yue, *Res. Astron. Astrophys.* **19**, 123 (2019).

[54] A. Tykhonov *et al.*, *Astropart. Phys.* **146**, 102795 (2023).

[55] Supplementary material available at <http://link.aps.org/supplemental/.../...> for charge reconstruction, background subtraction, effective acceptance, measured fluxes and systematic uncertainties.

[56] G. D. Lafferty and T. R. Wyatt, *Nucl. Instrum. Meth. A* **355**, 541 (1995).

[57] S. Abdollahi *et al.*, *Phys. Rev. D* **95**, 082007 (2017).

[58] C. Yue, P. X. Ma, M. Di Santo, L. B. Wu, F. Alemanno, P. Bernardini, D. Kyratzis, G. W. Yuan, Q. Yuan, and Y. L. Zhang, *Nucl. Instrum. Meth. A* **984**, 164645 (2020).

[59] J. B. Birks, *Proc. Phys. Soc. Sect. A* **64**, 874 (1951).

[60] Y. F. Wei, *IEEE Trans. Nucl. Sci.* **67**, 939 (2020).

[61] Y. F. Wei, Y. L. Zhang, Z. Y. Zhang, L. B. Wu, S. C. Wen, H. T. Dai, *et al.*, *Nucl. Instrum. Meth. A* **922**, 177 (2019).

[62] G. Dagostini, *Nucl. Instrum. Meth. A* **362**, 487 (1995).

[63] C. Kobayashi *et al.*, *Astrophys. J.* **900**, 179 (2020).

[64] C. Kobayashi, H. Umeda, K. Nomoto, N. Tominaga, and T. Ohkubo, *Astrophys. J.* **653**, 1145 (2006).

[65] K. Iwamoto, F. Brachwitz, K. Nomoto, N. Kishimoto, H. Umeda, *et al.*, *Astrophys. J. Suppl. Ser.* **125**, 439 (1999).

[66] K. Nomoto, F. K. Thielemann, and K. Yokoi, *Astrophys. J.* **286**, 644 (1984).

[67] F. Alemanno *et al.* (DAMPE), arXiv:2511.05409 .